Eddy current non destructive testing using an improved giant magnetoresistance magnetometer and a single wire as inducer : a FEM performance analysis

Rimond Hamia, Christophe Cordier, Sébastien Saez, Christophe Dolabdjian

Eddy-Current Nondestructive Testing Using an Improved GMR Magnetometer and a Single Wire as Inducer: A FEM Performance Analysis

Rimond Hamia, Christophe Cordier, Sébastien Saez, and Christophe Dolabdjian

GREYC UMR 6072-ENSICAEN and University of Caen Basse Normandie, 14050 Caen Cedex, France

This paper describes an efficient nondestructive evaluation (NDE) eddy-current (EC) system using an improved giant magnetoresistance magnetometer (IGMRM) and a simple single wire as inducer. A three-dimensional finite-element method (3-D FEM) was implemented to evaluate the theoretical expected response of the system. The model was based on a modified magnetic vector potential and a reduced magnetic scalar potential, in conducting and nonconducting regions, respectively. The model robustness is established by comparing numerical and experimental results on a given benchmark aluminum plate sample. This efficient 3-D FEM model helps to understand the system performances. Moreover, the excitation frequency effect on the sensed signal is analyzed versus the benchmark sample thickness and the crack sizes. Results are also given and discussed in terms of signal-to-noise ratio.

Index Terms—**Crack detection, eddy current, finite-element method, GMR, magnetometer, nondestructive testing.**

I. Introduction

THE eddy-current testing (ECT) method is widely used for nondestructive testing, inspection, and evaluation (NDT, NDI or NDE) of nuclear, aerospace, petroleum, and automotive industries, for example. In order to apply the ECT method to examine defects in the depths of the sample, it is necessary to use low-frequency magnetic field source as excitation. However, in these conditions, it is difficult for a conventional coil to sense a weak signal induced by a depth defect, because the coil sensitivity is poor [1], [2]. Ideally, low-frequency ECT methods require magnetic sensors having high field sensitivity, high spatial resolution, and low intrinsic magnetic noise in order to improve the signal-to-noise ratio (SNR) in that case.

The use of high sensitivity magnetic sensors leads to improve the defect detection in a nondestructive evaluation eddy-current system. Different types of magnetometers were implemented and tested in an EC state-of-the-art system, such as the superconducting quantum interference device (SQUID). SQUID is well-known as one of the most sensitive magnetometers, however, it is a prohibitive and a too complex object for industrial NDE system development [3]–[6]. Flux-gates are simple to operate, however, this technology is still expensive [7]. In addition, giant magnetoresistance (GMR) sensors combine a relatively high field sensitivity, a high spatial resolution [8], and a low cost and thus offer an optimum balance between the testing quality and the cost effectiveness.

In this study, we present a NDE system using IGMRM [24] which has been developed in the electronic team of the GREYC research group. Many state-of-the-art studies [9]–[12] have proposed systems for testing defects using a GMR sensor and show contributions of this technology in the detection of cracks by eddy-current testing. Nevertheless, we deplore the lack of good comparison between experimental and numerical results. For this reason, a 3-D FEM model was used to analyze the response from our NDE system. Further, the effects of the excitation frequency and crack size on the NDE system response are presented in order to give some elements of expected detection limit of this technology in a very simple benchmark design.

II. Description of the FEM Model

The numerical analysis of three-dimensional EC issues using FEM has been intensively studied during the past twenty years by numerous research groups concerned with computational electromagnetics. Various formulations were proposed for 3-D eddy-current analysis [13]–[17]. In NDT, the first challenge of that kind of calculation comes from the high numerical precision required to get the variation of the signal induced by defects versus other contributions. High precision can be obtained by mesh refinement, but in the case of magnetic vector formulation, the memory required for calculation increases and often exceeds the available computer RAM.

Here, we have implemented in COMSOL software [18] the well-known edge finite-element formulation $\boldsymbol{A}^*/\varphi_r$ [19], [20]. In this electromagnetic formulation, the modified magnetic vector potential $\boldsymbol{A}^*$ is associated to the reduced magnetic scalar potential φ_r. The vector potential $\boldsymbol{A}^*$ is only defined in the conducting region and is bound to the electric field $\boldsymbol{E}$ by

$$\boldsymbol{E} = -\frac{\partial \boldsymbol{A}^*}{\partial t} = -\frac{\partial \boldsymbol{A}}{\partial t} - \nabla V \tag{1}$$

where $\boldsymbol{A}$ and V are respectively the magnetic vector potential and the scalar electric potential. The magnetic flux density in the conducting plate is obtained from

$$\boldsymbol{B} = \nabla \times \boldsymbol{A}^*. \tag{2}$$

In the insulating region surrounding the aluminum sample, the magnetic field $\boldsymbol{H}$ is divided into two components

$$\boldsymbol{H} = \boldsymbol{H}_s + \boldsymbol{H}_r. \tag{3}$$

Each part is determined by

$$\nabla \times \boldsymbol{H}_s = \boldsymbol{J}_s \tag{4}$$

and

$$\boldsymbol{H}_r = -\nabla\varphi_r \tag{5}$$

respectively. The source field $\boldsymbol{H_s}$ corresponds to the field created by the current source $\boldsymbol{J_s}$ in the inducer and is calculated with the Biot-Savart's law. In our numerical analysis, it is merely given by

$$\boldsymbol{H}_s(x,y,z) = \frac{I}{2\pi(y^2+z^2)}(y\vec{e}_z - z\vec{e}_y) \tag{6}$$

where $\overrightarrow{e}_i$ is the unit vector codirected with the i-axis and I is the current amplitude in the inducer.

The field $\boldsymbol{H_r}$ is the magnetic response of the conducting region to the source field. It is derived from the reduced magnetic scalar potential φ_r. In order to calculate the potential $\boldsymbol{A}^*$ and φ_r, we have to consider the Maxwell-Ampere equation in the quasi-stationary state and the divergence free nature of the magnetic flux density. Finally, in order to get the magnetic flux density $\boldsymbol{B}$ on the whole space domain, we solve (7), in region with eddy current, and (8), in nonconducting region. It gives, with the usual notations

$$\nabla \times \left[(\mu_0\mu_r)^{-1}\nabla \times \boldsymbol{A}^*\right] + j\omega\sigma\boldsymbol{A}^* = 0 \tag{7}$$

$$\nabla \cdot [\mu_0\mu_r\nabla\varphi_r] = 0. \tag{8}$$

The potentials $\boldsymbol{A}^*$ and φ_r are coupled in the weak form of (6) and (7) thanks to the appropriate surface integrals over the boundary between the conducting and insulating region.

In order to reduce the degrees of freedom in the nonconducting region, we used a scalar potential instead of a vector one. Moreover, with a reduced potential there is no need to discretize the inducer with finite element [21]. Only the interfaces between conductors and insulators must be discretized with care, especially when inducers are close to the sample. For these reasons, it is recommended to use a reduced scalar potential. Indeed, this formulation is an efficient mean to get the required accuracy for describing defect response in NDT problems. The mesh around the sensor positions can be refined without extensive numerical cost. Only the response of the sample to $\boldsymbol{H_s}$ is computed near the sensor with the FEM. Furthermore, NDE scans can be done without meshing the geometry for each inducer position. Thus, this method avoids numerical noise due to mesh variability.

Notice that additional techniques must be implemented with this formulation in order to deal with multiply connected conductors [22], [23].

III. Theoretical to Experimental Comparison

A. Eddy-Current System

A NDE setup is used to assess the performances of a IGMRM [24] dedicated to the measurement of deep lying cracks in conducting materials. Previously, the performances of this magnetometer was studied and compared to classical ones. It was also implemented and tested in different kinds of eddy-current systems [24], [25].

IGMRM [24] has very interesting characteristics for eddy-current NDE in shielded and unshielded environment. For example, its high slew rate permits a high magnetic field disturbance rejection which appears in industrial environment. Moreover, the dynamic range measurement of this magnetometer is intrinsically higher than 60 to 80 dB compared to classical systems for a frequency range from 10 Hz to 10 kHz [26]. All these characteristics and other ones, like sensitivity, 1000 V/T, bandwidth, 100 kHz, white noise level, 50 $\mathrm{pT}/\sqrt{\mathrm{Hz}}$ and 1/f noise corner frequency of 4 kHz, make this kind of magnetometer very promising as a punctual sensor [27], [28], compared to classical coil sensor.

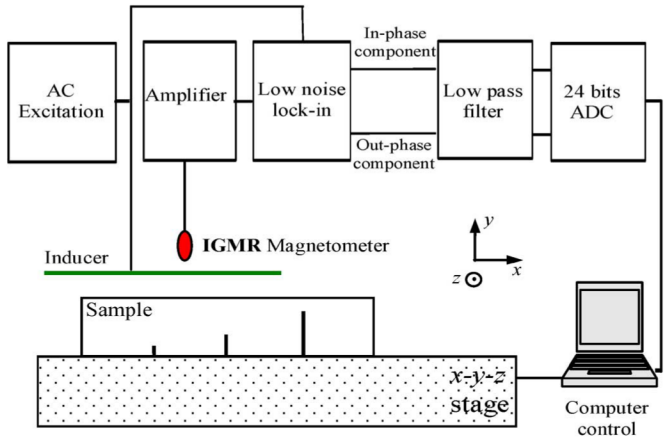

Fig. 1. Sketch view of the nondestructive evaluation implemented system.

Fig. 1 shows the used experimental setup. It consists of an IGMRM oriented so as to detect the tangential component of magnetic field, B_x, appearing near the inducer (50 cm long). The latest is made of a single wire inducer which is fed by a sinusoidal current at the frequency, f, and an amplitude, I.

The magnetometer output voltage is amplified and then synchronously demodulated by a low-noise dual channel lock-in amplifier which gives the in-phase and the out-phase voltage components corresponding to the magnetic flux density sensed by the IGMRM. These two demodulated outputs are then low pass filtered and acquired by a 24 bit analog to digital converter (ADC). The data acquisition and the x-y-z scanning stages are software controlled.

In our setup, as given in Fig. 1, the inducer and the magnetometer are totally decoupled providing high system implementation flexibility in terms of design and geometry. IGMR array [29] can share only one inducer for large surface scanning. In addition, this kind of multi-head sensor avoids problems of crosstalk commonly encountered with classical coil sensors. The use of a current line excitation is very practical as its length and shape can be easily adapted to a target application.

B. Numerical and Experimental Result Comparison

A benchmark simulation is initially carried out to verify the accuracy of the 3-D FEM model by comparison with experimental measurements. Present results were made on a benchmark aluminum sample plate (16 cm × 5 cm × 1 cm) with three machined subsurface cracks (Forster ref. 2.899.01-9303-0005), as shown in Fig. 2. The defect sizes are given in Table I. In this benchmark, the inducer length was not optimized for the crack detection. In order to simplify the numerical simulations, we have chosen a very long line that can be considered as infinite in the model.

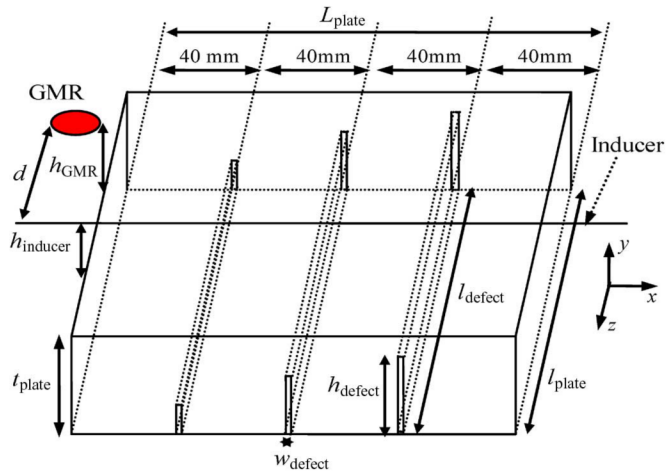

Fig. 2. Sketch view of the used benchmark aluminum sample plate with associated subsurface cracks ($L_{plate} = 160$ mm, $l_{plate} = 50$ mm, $t_{plate} = 10$ mm). Defect sizes are given in Table I.

TABLE I
BENCHMARK SAMPLE PLATE CRACK SIZES

Subsurface defect	Length l_{defect} [mm]	Width w_{defect} [µm]	Height h_{defect} [mm]
N°1	50	500	2
N°2	50	500	4
N°3	50	500	8

First measurement was done at an inducer current frequency and amplitude of 450 Hz and 180 mA, respectively. The lift-offs of the inducer and the IGMRM over the sample are 1 and 2 mm, respectively. Details are given in Fig. 2. The sensing axis of the magnetometer is set in x-axis, parallel to the scanning direction, in order to sense the magnetic flux density component, B_x.

Numerical simulation is performed with the PARDISO solver with two quad-core processors (Intel Xeon X5472 at 3 GHz) and 64 GB of RAM. The geometry of the problem is discretized with tetrahedral elements which lead approximately to 1 070 000 degrees of freedom. The CPU time needed to solve the problem is 602 s. The robust solution is given by a very high-quality dense mesh and does not vary when slight mesh variations are done.

Figs. 3 and 4 show numerical and experimental B_x components, its modulus and the associated Lissajous curves, respectively. Both depend on the axial position of the magnetometer, x. The results show that the proposed EC system is able to easily detect all benchmark sample subsurface cracks. The sensed signal amplitude is proportional to crack size and depth. Moreover, unlike conventional coil system, the wide IGMRM dynamic range measurement allows to sense the sample edges and cracks, in a same scan. Also, results mean that the IGMRM used is able to detect subsurface crack even if the lift-off is high (2 mm, as given in Fig. 1). In the simulations, the conductivity of the sample and the lift-off of the sensor have been adjusted to roughly fit to the experimental results. In the numerical model, the used conductivity is equal to 1.68×10^7 S/m, which is in agreement with the aluminum one. Similarly, the lift-off h_{GMR} is fixed to 2.2 mm, which is closed to the experimental one, if

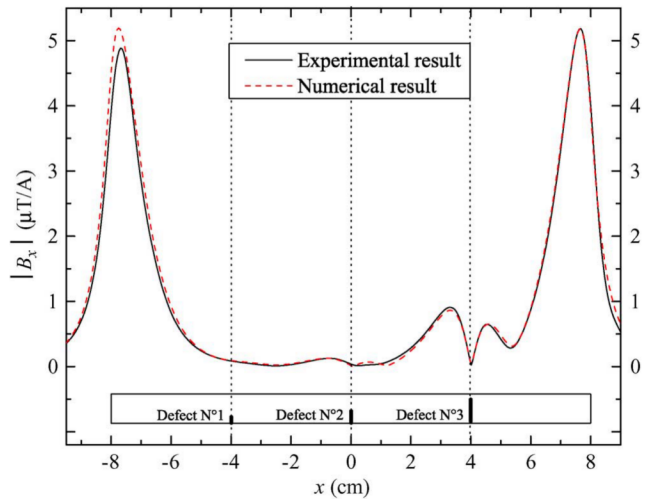

Fig. 3. Numerical and experimental magnetic field component modulus, $|B_x|$, sensed on the sample plate shown in Fig. 2, versus the axial magnetometer position, x. Results are given in tesla per ampere as they have been normalized by I. ($d = 12$ mm, $h_{inducer} \approx 1$ mm, $h_{GMR} \approx 2$ mm, $t_{plate} = 10$ mm, $f = 450$ Hz). In simulations, $h_{GMR} = 2.2$ mm and $\sigma = 1.68 \times 10^7$ S/m.

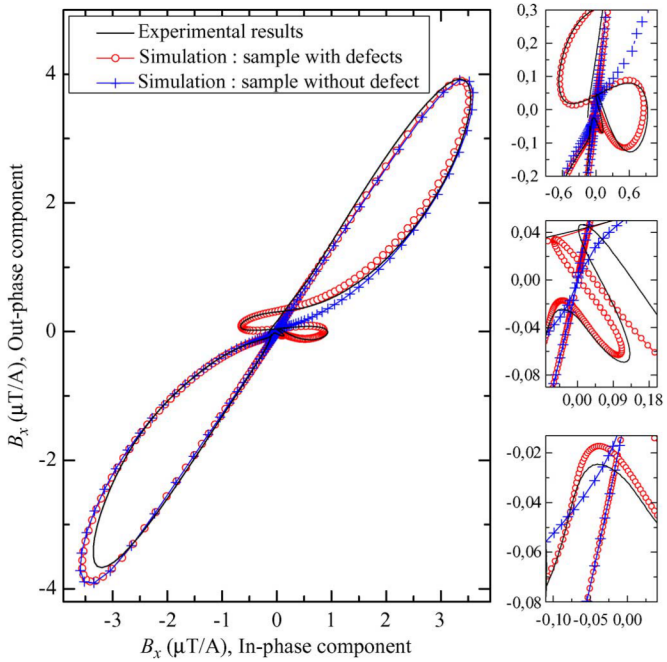

Fig. 4. Numerical and experimental Lissajous curve comparison of magnetic field component per ampere, B_x/I, sensed on the benchmark sample plate (cf. Fig. 2), versus x axis scanning. Insets give in detail the response induced by each sample defect (cf. Table I). ($d = 12$ mm, $h_{inducer} \approx 1$ mm, $h_{GMR} \approx 2$ mm, $t_{plate} = 10$ mm, $f = 450$ Hz). In simulations, $h_{GMR} = 2.2$ mm and $\sigma = 1.68 \times 10^7$ S/m.

we take into account the setup mechanical precision. The relative errors between measurement and simulation are represented on Fig. 5 for the modulus $|B_x|$ and the phase φ_x of B_x. They are given by

$$\varphi_{x,\text{relative error}} = \frac{\varphi_{x,\text{measurement}} - \varphi_{x,\text{simulation}}}{\varphi_{x,\text{measurement}}} \quad (9)$$

$$|B_x|_{\text{relative error}} = \frac{|B_x|_{\text{measurement}} - |B_x|_{\text{simulation}}}{|B_x|_{\text{measurement}}}. \quad (10)$$

These errors are lower than 25% above the sample edges and above the defects number 1 and 3. This means that simulation

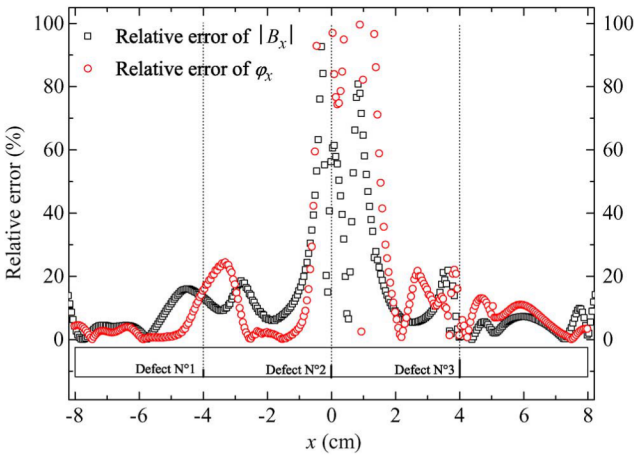

Fig. 5. Relative error between measurement and simulation in the respect of Fig. 4 for the modulus $|B_x|$ and the phase φ_x of B_x, versus x axis scanning.

succeeds in describing qualitatively and quantitatively experimental results. We still observe a slight difference between numerical and experimental curves mainly induced by mismatch between some experimental and simulation parameters. Fig. 5 shows that the relative error above defect number 2 can reach 100% which only represents a maximum absolute error of 70 nT. Although, the Lissajous curve above defect number 2 is qualitatively well described by simulation, the numerical model fails to precisely fit the response of this defect. In order to estimate the influence of the model parameters, we have calculated, above defects, the maximum magnetic flux density modulus and phase variations, written $\delta|B_x|_m$ and $\delta\varphi_{xm}$, respectively, versus the variation of several simulation parameters. In Fig. 6, numerical parameters have been increased and decreased by 10%, 20%, 40%, and 60% compared to the ones used in the previous model. The distance d between the magnetometer and the inducer has more influence on B_x than the other geometric parameters. On the contrary, variations of h_{inducer} do not modify B_x significantly. Uniform variations of d, h_{GMR} and σ, can explain the relative error between measurement and simulation above the plate edges and the defects number 1 and 3. The whole error above defect number 2 is reasonably due to the addition of error from the conductivity and the geometric parameters, which are supposed uniform in the model, and crosstalk between defect magnetic signatures.

To summarize the good agreement between simulation and measurement, for the most part of the results, validates the 3-D FEM simulation model, and implies the possibility of using the numerical simulation to analyze system performances versus excitation frequency, crack sizes and lift-off, on the sensed EC signal as given hereinafter.

IV. EC Testing Performance Analysis With the Help of the 3-D FEM

In the scope of this work, calculations were performed with and without cracks in order to evaluate the highest signal induced by defect in term of amplitude, $|\Delta B_i|$, with an associated phase, $\Delta\varphi_i$. Both of these parameters depend mainly on the excitation frequency and sensor position on sample under test. In

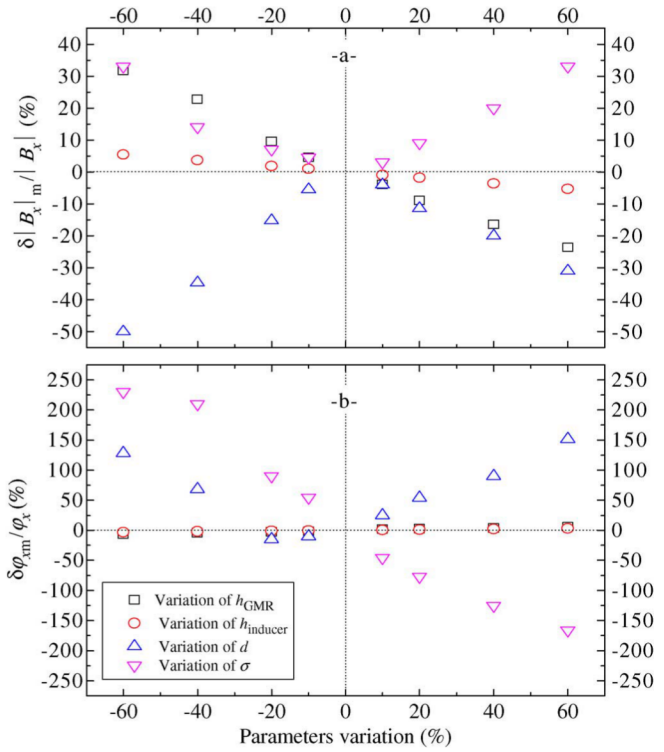

Fig. 6. Relative variation of $\delta|B_x|_m$ (a) and $\delta\varphi_{xm}$ (b), versus the variation of the model parameters compared to the initial simulation ones (h_{GMR}, h_{inducer}, d and σ).

order to match the experimental setup, the inducer and the magnetometer were set at a lift-off of 1 mm and 2.2 mm, respectively. In the cases with and without flaw, the meshes are slightly different in the defects region. Nevertheless, it has a negligible impact on the results because the meshes are dense and identical in the critical region where the magnetometer is positioned.

Miscellaneous equations are defined by

$$|\Delta B_x(f)| = \text{Max}\,||B_{x,\text{crack}}(f,x)| - |B_{x,0}(f,x)|| \qquad (11)$$

and associated normalized value

$$\text{Norm}\,(|\Delta B_x|) = \frac{|\Delta B_x(f)|}{|\Delta B_x(f_{\text{opt}})|} \qquad (12)$$

where $B_{x,\text{crack}}$ and $B_{x,0}$ are the magnetic flux density, sensed along the x-axis, at the magnetometer location, with and without cracks, respectively. f_{opt} is named the optimal excitation frequency and induces the highest magnetic field defect amplitude signature of $|\Delta B_x(f)|$. The associated parametric curves of $\text{Norm}(|\Delta B_x|)$ versus frequency are given for some configurations in Figs. 7, 8, and 9. The frequency ranges from some Hz to kHz.

A. Sensed Signal Amplitude Behavior Versus Excitation Frequency

When attempting to locate a subsurface crack, a frequency is often selected to insure that the strength of the eddy current will be sufficient at the defect depth to produce a measurable magnetic field signature.

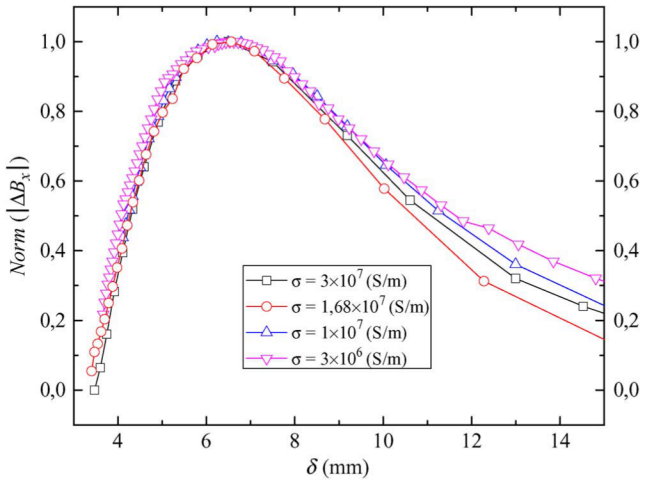

Fig. 7. Numerical evaluation of the normalized highest magnetic field component, $\mathrm{Norm}(|\Delta B_x|)$, versus the skin depth for 4 plate electrical conductivity values. ($d = 12$ mm, $h_{\mathrm{inducer}} = 1$ mm, $h_{\mathrm{GMR}} = 2.2$ mm, $t_{\mathrm{plate}} = 10$ mm, $w_{\mathrm{defect}} = 0.5$ mm, $l_{\mathrm{defect}} = 50$ mm, $h_{\mathrm{defect}} = 1$ mm).

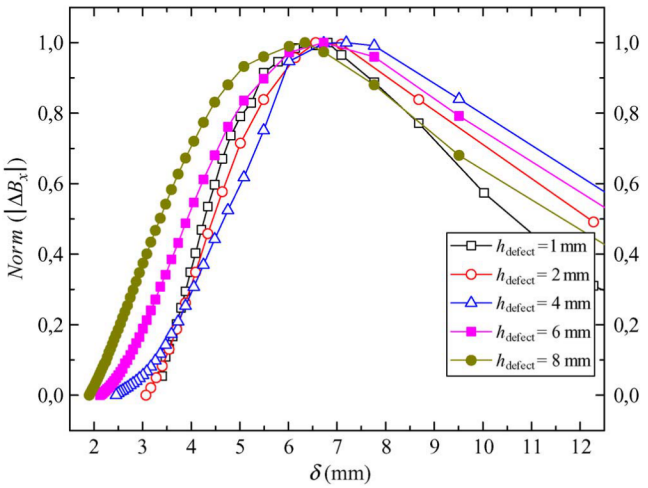

Fig. 8. Numerical evaluation of the normalized highest magnetic field component, $\mathrm{Norm}(|\Delta B_x|)$, versus the skin depth for 6 crack heights. ($d = 12$ mm, $h_{\mathrm{inducer}} = 1$ mm, $h_{\mathrm{GMR}} = 2.2$ mm, $\sigma = 1.68{\times}10^7$ S/m, $t_{\mathrm{plate}} = 10$ mm, $w_{\mathrm{defect}} = 0.5$ mm, $l_{\mathrm{defect}} = 50$ mm).

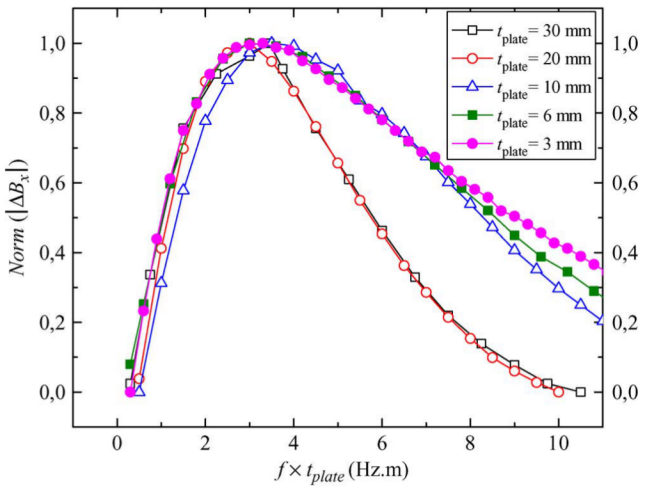

Fig. 9. Variation of the $\mathrm{Norm}(|\Delta B_x|)$ signal as a function of the excitation frequency and plate thickness product ($d = 12$ mm, $h_{\mathrm{inducer}} = 1$ mm, $h_{\mathrm{GMR}} = 2.2$ mm, $\sigma = 1.68 \times 10^7$ S/m, $w_{\mathrm{defect}} = 0.5$ mm, $l_{\mathrm{defect}} = 50$ mm, $h_{\mathrm{defect}} = 10\%$ of the plate thickness).

In conductor, the decay of the eddy current is governed by the skin depth or the penetration depth which is

$$\delta = \sqrt{\frac{1}{\pi f \mu \sigma}} \tag{13}$$

where σ, μ are the electrical conductivity and the magnetic conductivity of the sample, respectively. The penetration depth value gives an idea on the required detection frequency versus the sample thickness. The related expected frequency dependency is roughly given by

$$f \propto \frac{1}{t_{\mathrm{plate}}^2}. \tag{14}$$

We study, with the help of the FEM, the effect of the excitation frequency on alike external benchmark sample plate size (16 cm × 5 cm × 1 cm) with only one centered subsurface crack. Its length, width and height are 50 mm, 0.5 mm, and 1 mm, respectively. The magnetic conductivity of the sample is μ_0. Fig. 7 gives the expected and normalized sensed signal amplitude, $\mathrm{Norm}(|\Delta B_x|)$, dependence versus the skin depth (Cf. (13)) for different electrical sample conductivities.

An important comment issues from the plot observation. Indeed, for a 10 mm plate thickness and an electrical conductivity ranging from 0.3×10^7 to 3×10^7 S/m, the normalized sensed signal amplitude, $\mathrm{Norm}(|\Delta B_x|)$, is maximal when the skin depth reaches an optimal value, approximately equal to 6.5 mm. Consequently, related to sample plate thickness and conductivity, an optimal excitation frequency, f_{opt}, exists for the best defect amplitude signature measurements. For our aluminum sample ($\sigma = 1.68 \times 10^7$ S/m, $t_{\mathrm{plate}} = 10$ mm), the optimal frequency is around 325 Hz.

B. Sensed Signal Amplitude Behavior Versus Crack Height

Fig. 8 plots show the relation between the normalized amplitude of the sensed signal, $\mathrm{Norm}(|\Delta B_x|)$, versus the skin depth for different crack height values. Similar parameters are used as before, except for electrical conductivity (1.68×10^7 S/m). The crack heights h_{defect} range from 1 to 8 mm. As shown, the signal is maximized for a skin depth of around 6–7 mm. This range includes the value given previously. Moreover, the optimal excitation frequency is practically invariant in spite of the various crack height values. Also, we conclude that, regardless of the subsurface crack height, an optimal excitation frequency exits for a given thickness sample plate.

C. Optimal Frequency Versus Plate Thickness

Subsequently, the optimal excitation frequency was examined versus the plate thickness. Here, the electrical plate conductivity is 1.68×10^7 S/m and the centered subsurface crack height is set at 10% of t_{plate}. The crack width and length were kept constant as 0.5 mm and 50 mm, respectively. As given in Fig. 9, the optimal excitation frequency that maximizes the sensed signal, $\mathrm{Norm}(|\Delta B_x|)$, changes with the sample plate thickness. The optimal frequency and sample thickness product appears constant for the highest sensed signal.

The existence of an optimal frequency excitation for subsurface defect detection can be explained with simple considerations related to the distribution and the amplitude of the induced

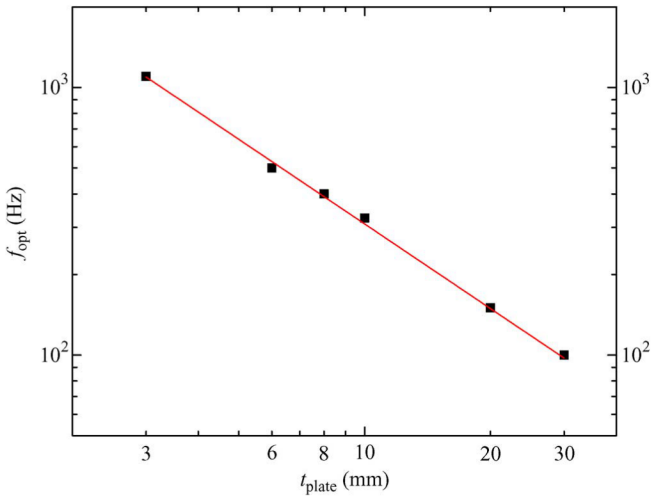

Fig. 10. Relationship between the optimum frequency $f_{\rm opt}$ and the thickness of plate ($d = 12$ mm, $h_{\rm inducer} = 1$ mm, $h_{\rm GMR} = 2.2$ mm, $\sigma = 1.68 \times 10^7$ S/m, $w_{\rm defect} = 0.5$ mm, $l_{\rm defect} = 50$ mm, $h_{\rm defect} = 10\%$ of the plate thickness). The line gives one over $t_{\rm plate}$ slope dependence.

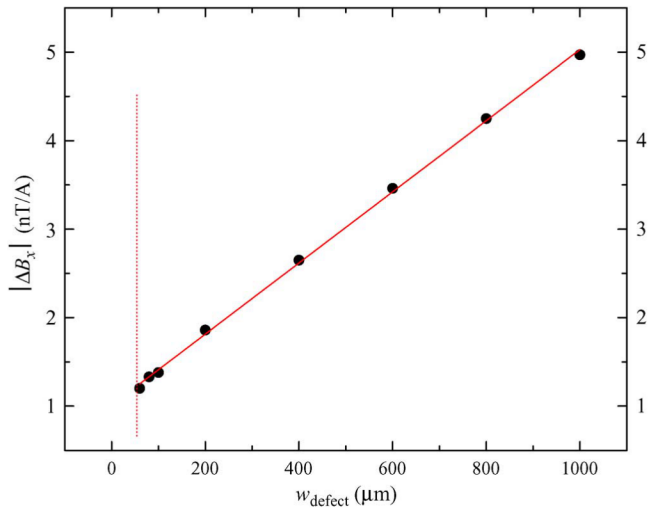

Fig. 11. Effect of the crack width on the sensed signal, $|\Delta B_x|$. The vertical dashed line gives the present limits of numerical simulation. The line shows that the sensed signal is proportional to $w_{\rm defect}$ for a given crack height. ($f_0 = 325$ Hz, $d = 12$ mm, $h_{\rm inducer} = 1$ mm, $h_{\rm GMR} = 2.2$ mm, $\sigma = 1.68 \times 10^7$ S/m, $l_{\rm defect} = 50$ mm, $h_{\rm defect} = 1$ mm, $t_{\rm plate} = 10$ mm).

current in the plate. First, we know that low frequency implies a deep eddy-current penetration, whereas high frequency implies a reduced eddy-current penetration depth, and therefore poor buried crack detection. Secondly, according to the Faraday's law, the eddy-current amplitude tends to increase with the excitation frequency. Consequently, these two effects explained the existence of an intermediate frequency that is optimal for the detection of subsurface crack.

The relationship between optimal frequency and the sample thickness is given in Fig. 10. It shows that, considering our analysis, $f_{\rm opt}$ depends on $1/t_{\rm plate}$, contrary to what one might think (cf. (14)).

D. From Sensed Signal Amplitude Versus Crack Sizes to SNR Evaluation

The effect of the size crack on the sensed signal, $|\Delta B_x|$, was investigated using an optimal excitation current frequency of 325 Hz.

The amplitude variation of the signal (referred to the excitation current amplitude), $|\Delta B_x|$, versus the crack width, $w_{\rm defect}$, is given in Fig. 11. The crack height, and length were kept constant at 1 and 50 mm, respectively. The crack width has a slight influence on the sensed signal amplitude, $|\Delta B_x|$. In theory, the detection of the crack seems possible even for small crack width of some hundred of μm. However, the detection ability of the system depends mainly on its mechanical stabilities and excitation current amplitude, I.

The amplitude variation of the signal, $|\Delta B_x|$, versus the crack height $h_{\rm defect}$ is given in Fig. 12. Two slopes associated to linear-logarithm dependence are observed. It shows that $|\Delta B_x|$ amplitude slowly decreases versus the crack height. More, at an excitation frequency of 325 Hz and a post synchronous detector low pass filter of 1 Hz bandwidth, the IGMRM noise level is around 0.53 $\rm nT_{Peak}$. It provides theoretically a good intrinsic signal-to-noise ratio (SNR) in the given experimental example, as detailed in Fig. 12. For an excitation current amplitude of 1 A, the sensed signal appears to be higher than the IGMRM

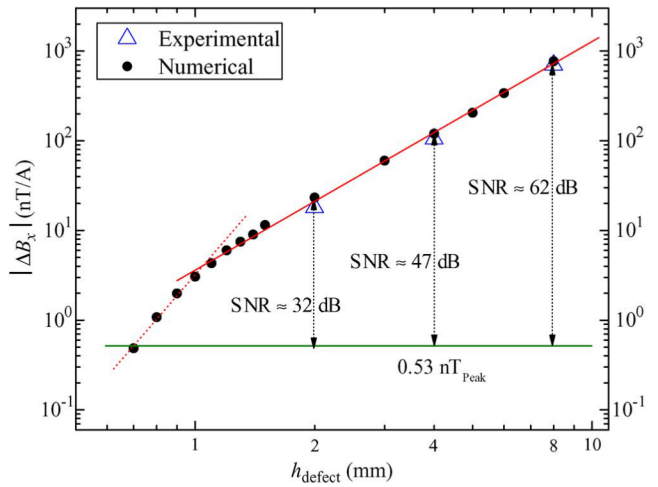

Fig. 12. Effect of the crack height on the signal amplitude, $|\Delta B_x|$. The horizontal line gives the peak noise level amplitude of the IGMRM as detailed previously. The triangles give experimental measured values referred to Figs. 3 and 4. The associated SNR are given for an excitation current amplitude I of 1 A. ($f_0 = 325$ Hz, $d = 12$ mm, $h_{\rm inducer} = 1$ mm, $h_{\rm GMR} = 2.2$ mm, $\sigma = 1.68 \times 10^7$ S/m, $l_{\rm defect} = 50$ mm, $w_{\rm defect} = 0.5$ mm).

intrinsic noise for a height higher than 700 μm. In decibels, SNR versus $h_{\rm defect}$ (given in μm) fit to

$$\mathrm{SNR} \approx 20\,(0.87 + 2.49\mathrm{Log}[h_{\rm defect}] - \mathrm{Log}[I])\,\mathrm{dB} \qquad (15)$$

with $h_{\rm defect}$ higher than 1.1 mm and

$$\mathrm{SNR} \approx 20\,(0.77 + 4.83\mathrm{Log}[h_{\rm defect}] - \mathrm{Log}[I])\,\mathrm{dB} \qquad (16)$$

with $h_{\rm defect}$ lower than 1.1 mm.

However, these results have to be balanced by some variation parameters depending on the scanning or on the environment, like lift-off, edge effect and true environmental magnetic field noise, for example. The latest easily rises to few 100 $\rm nT_{Peak}$ in our laboratory environment but could be rejected by gradiometric configuration. Furthermore, it seems possible to easily detect a subsurface crack in a high dynamic range as 120 dB,

even if the crack height is small as 5%–10% of the thickness of the plate. Nevertheless, it has to be balanced by the ability to distinguish the subsurface crack versus edge effect, as an example. In this case, the difficulty is to separate the high response of the edge from the small one of the crack. These two elements can be closed to each other whereas the measurement system cannot be brought closer to the defect.

V. Conclusion

A 3-D finite-element model was implemented and applied to evaluate the detection performance of a benchmark NDE eddy-current system using an IGMRM. The validity of the numerical results shows the capability of 3-D FEM to predict crack magnetic field signature in conducting sample. The results show the existence of an optimal frequency for subsurface crack detection mainly related to the sample plate thickness and conductivity. We have evaluated the SNR of our system in the case of an aluminum sample plate. A good fit between theoretical results and experimental measurements was observed.

High sensitivity magnetometers, like IGMRM, have a key place in the field of NDT magnetic applications. The IGMRM measuring range and spatial resolution place this sensor between inexpensive Hall sensor and expensive SQUID system. Also, it offers new modular capabilities, simplicity and low cost probe developments. Moreover, its high slew rate gives them a high potential for harsh NDE industrial electromagnetic environment working place.

References

[1] Y. Cha, K. H. Kim, J. Shon, Y. H. Kim, and J. Kim, "Surface flaws detection using AC magnetic field sensing by a thin film inductive microsensor," *IEEE Trans. Magn.*, vol. 44, no. 11, pp. 4022–4025, Nov. 2008.

[2] C. Cordier, S. Saez, S. Lebargy, and C. Dolabdjian, "Accurate steel tube axis alignment in nondestructive evaluation probe," *IEEE Trans. Magn.*, vol. 44, no. 10, pp. 2409–2413, Oct. 2008.

[3] Y. Hatsukade, S. Okumo, K. Mori, and S. Tanaka, "Eddy-current-based SQUID-NDE for detection of surface flaws on copper tubes," *IEEE Trans. Appl. Supercond.*, vol. 17, no. 2, pp. 780–783, Jun. 2007.

[4] S. Hirano, Y. Inada, E. Matsumoto, A. Saito, K. Aizawa, M. Matsuda, S. Kuriki, and S. Ohshima, "SQUID nondestructive testing system with vibrating normal pick-up coil," *IEEE Trans. Appl. Supercond.*, vol. 17, no. 2, pp. 788–791, Jun. 2007.

[5] T. Q. Yang, K. Yao, D. Yamasaki, and K. Enpuku, "Eddy current testing utilizing normal pickup coil and superconducting quantum interference device picovoltmeter," *Jpn. J. Appl. Phys.*, vol. 44, no. 35, pp. L1128–L1130, Jun. 2007.

[6] H. H. Qi, P. L. Lang, M. J. Zhang, T. S. Wang, D. N. Zheng, and Y. J. Tian, "High-Tc dc-SQUID magnetometer and its application in eddy current non-destructive evaluation," *Cryogenics*, vol. 44, pp. 695–699, 2004.

[7] P. Ripka, "Advances in fluxgate sensors," *Sens. Actuators A: Phys.*, vol. 106, no. 1–3, pp. 8–14, Sep. 15, 2003.

[8] L. Perez, C. Dolabdjian, W. Waché, and L. Butin, "Advance in magnetoresistance magnetometer performances applied in eddy current sensor arrays," presented at the 16th World Conf. NDT, Montreal, QC, Canada, 2004.

[9] K. Tsukada, T. Kiwa, T. Kawata, and Y. Ishihara, "Low-frequency eddy current imaging using MR sensor detecting tangential magnetic field components for nondestructive evaluation," *IEEE Trans. Magn.*, vol. 42, no. 10, pp. 3315–3317, Oct. 2006.

[10] K. Chomsuwan, S. Yamada, M. Iwahara, H. Wakiwaka, and S. Shoji, "Application of eddy current testing technique for high-density double-layer printed circuit board inspection," *IEEE Trans. Magn.*, vol. 41, no. 10, pp. 3619–3321, Oct. 2005.

[11] N. V. Nair, V. R. Melapudi, H. R. Jimenez, X. Liu, Y. Deng, Z. Zeng, L. Udpa, T. J. Moran, and S. S. Udpa, "A GMR-based eddy current system for NDE of aircraft structures," *IEEE Trans. Magn.*, vol. 42, no. 10, pp. 3312–3314, Oct. 2006.

[12] J. T. Jeng, G. S. Lee, W. C. Liao, and C. L. Shu, "Depth-resolved eddy current detection with GMR magnetometer," *J. Magn. Magn. Mater.*, vol. 304, pp. e470–e473, Oct. 2006.

[13] O. Biro and K. Preis, "On the use of the magnetic vector potential in the finite element analysis of three-dimensional eddy currents," *IEEE Trans. Magn.*, vol. 25, no. 4, pp. 3145–3159, Jul. 1989.

[14] O. Biro and K. Preis, "Finite element analysis of 3D eddy currents," *IEEE Trans. Magn.*, vol. 26, no. l2, pp. 418–423, 1990.

[15] O. Biro, "Edge element formulations of eddy current problems," *Comput. Meth. Appl. Mech. Eng.*, vol. 169, pp. 391–405, 1999.

[16] G. Rubinacci, A. Tamburrino, and S. Ventre, "An efficient numerical model for a magnetic core eddy-current probe," *IEEE Trans. Magn.*, vol. 44, no. 6, pp. 1306–1309, Jun. 2008.

[17] R. V. Sabariego and P. Dular, "A perturbation approach for the modeling of eddy current nondestructive testing problems with differential probes," *IEEE Trans. Magn.*, vol. 43, no. 4, pp. 1289–1292, Apr. 2007.

[18] COMSOL Multiphysics software [Online]. Available: http://www.comsol.com/

[19] C. R. I. Emson and J. Simkin, "An optimal method for 3D eddy currents," *IEEE Trans. Magn.*, vol. 19, no. MAG-6, pp. 2450–2452, Nov. 1983.

[20] J. Simkin, "Eddy current modelling in three dimensions," *IEEE Trans. Magn.*, vol. 22, no. MAG-5, pp. 609–613, Sep. 1986.

[21] Z. Zeng, L. Udpa, S. S. Udpa, and M. S. C. Chan, "Reduced magnetic vector potential formulation in the finite element analysis of eddy current nondestructive testing," *IEEE Trans. Magn.*, vol. 45, no. 3, pp. 964–967, Mar. 2009.

[22] T. Morisue, "A new formulation of the magnetic vector potential method in 3-D multiply connected regions," *IEEE Trans. Magn.*, vol. 24, no. 1, pp. 90–93, Jan. 1988.

[23] O. Biro, K. Preis, and W. Renhart, "Finite element analysis of 3D multiply connected eddy current problems," *IEEE Trans. Magn.*, vol. 25, no. 5, pp. 4009–4011, Sep. 1989.

[24] L. Perez, C. Dolabdjian, G. Waché, and L. Butin, "Advance in magnetoresistance magnetometer performances applied in eddy current sensor arrays," presented at the 16th WCNDT'04 Conf., Montréal, QC, Canada, Aug. 28–Sep. 3, 2004.

[25] C. Dolabdjian, G. Waché, and L. Perez, "Improvement in subsurface fatigue cracks under airframes fasteners detection using improved rotary giant magnetoresistance magnetometer head," *Insight—Non-Destruct. Test. Cond. Monitor.*, vol. 49, no. 2, pp. 133–136, 2007.

[26] C. Dolabdjian, L. Perez, V. O. de Haan, and P. A. de Jong, "Performance of magnetic pulsed eddy current system using high dynamic and high linearity improved giant magnetoresistance," *IEEE Sensors J.*, vol. 6, no. 6, pp. 1511–1517, 2006.

[27] C. Dolabdjian, A. Qasimi, and D. Bloyet *et al.*, "Spatial resolution of SQUID magnetometers and comparison with low noise room temperature magnetic sensors," *Physica C—Supercond. Appl.*, vol. 368, no. 1–4, pp. 80–84, 2002.

[28] R. Hamia, C. Cordier, S. Saez, and C. Dolabdjian, "Giant magneto impedance sensor for non destructive evaluation eddy current system," *Sensor Lett.*, vol. 7, no. 3, pp. 437–441, 2009.

[29] G. Waché, L. Butin, L. Perez, and C. Dolabdjian, "NDE perspectives with magnetoresistance array technologies. From research to industrial applications," *Insight—Non-Destruct. Test. Cond. Monitor.*, vol. 47, no. 5, pp. 280–284, 2005.